

DeepGeoS: A Deep Interactive Geodesic Framework for Medical Image Segmentation

Guotai Wang, Maria A. Zuluaga, Wenqi Li, Rosalind Pratt, Premal A. Patel, Michael Aertsen, Tom Doel, Anna L. David, Jan Deprest, Sébastien Ourselin, Tom Vercauteren

Abstract—Accurate medical image segmentation is essential for diagnosis, surgical planning and many other applications. Convolutional Neural Networks (CNNs) have shown to be state-of-the-art automatic segmentation methods while the result still needs to be refined to become accurate and robust enough for clinical use. We propose a deep learning-based interactive segmentation method in order to improve the segmentation obtained by an automatic CNN as well as reduce user interactions during refinement for better results. We use one CNN to obtain an initial segmentation automatically, on which user interactions are added to indicate mis-segmentations. Another CNN takes as input the user interactions with the initial segmentation and gives a refined result. We propose a new way to combine user interactions with CNNs through geodesic distance maps, and propose a resolution-preserving network that can give better dense prediction. In addition, we integrate user interactions as hard constraints into back-propagatable Conditional Random Fields. We validated the proposed framework in the application of placenta segmentation from fetal MRI and clavicle segmentation from chest radiographs. Experimental results show our method achieves a large improvement from automatic CNNs, and obtains comparable accuracy with fewer user interventions and less time compared with traditional interactive methods.

Index Terms—Interactive image segmentation, convolutional neural network, geodesic distance, conditional random fields

1 INTRODUCTION

SEGMENTATION of anatomical structures is an essential task for a range of medical image processing applications such as image-based diagnosis, anatomical structure modeling, surgical planning and guidance. Although automatic segmentation methods [1] have been investigated for many years, they can rarely achieve sufficiently accurate and robust results to be useful for many medical imaging applications. This is mainly due to poor image quality (with noise, artifacts and low contrast), large variations among patients, inhomogeneous appearances brought by pathology, and variability of protocols among clinicians leading to different definitions of a given structure boundary. Interactive segmentation methods, which take advantage of users' knowledge of anatomy and the clinical question to overcome the challenges faced by automatic methods, are widely used for higher accuracy and robustness [2].

Although leveraging user interactions helps to obtain more precise segmentation results [3], [4], [5], [6], the resulting requirement for many user interactions increases the burden on the user. Thus, a good interactive segmentation method should require as few user interactions as possible, leading to interaction efficiency. Machine learning methods are commonly used to reduce user interactions. For example, GrabCut [7] uses Gaussian Mixture Models to model color distribution and only requires the user to provide a bounding box. SlicSeg [8] employs Online Random Forests to segment a Magnetic Resonance Imaging (MRI) volume

by learning from user-provided scribbles in only one slice. Active learning is used in [9] to actively select candidate regions for querying the user.

Recently, deep learning techniques with convolutional neural networks (CNNs) have achieved increasing success in image segmentation [10], [11], [12]. They can find the most suitable features through automatic learning instead of manual design. By learning from large amounts of training data, CNNs have achieved state-of-the-art performance for automatic segmentation [12], [13], [14]. One of the most widely used methods is Fully Convolutional Network (FCN) [11]. It outputs the segmentation directly by computing forward propagation only once at testing time.

Recent advances of CNNs for image segmentation mainly focus on two aspects. The first is to overcome the problem of reduction of resolution caused by repeated combination of max-pooling and downsampling. Though some upsampling layers can be used to recover the resolution, this easily leads to blob-like segmentation results and low accuracy for tiny structures [11]. In [12], [15], dilated convolution is proposed to replace some downsampling layers. Dilated convolution allows exponential expansion of the receptive field without loss of resolution. However, the CNNs in [12], [15] keep three layers of pooling and downsampling therefore their output resolution is still reduced eight times compared with the input. The second aspect is to enforce inter-pixel dependency to get a spatially regularized result. This helps to recover edge details and reduce noise in pixel classification. DeepLab [16] used fully connected Conditional Random Fields (CRFs) as a post processing step. But its parameters rely on manual tuning which is time-consuming and may not ensure optimal values. It was shown in [17] that the CRF can be formulated as a Recurrent Neural Network (RNN) so that it can be trained end-to-

- G. Wang, M.A. Zuluaga, W. Li, R. Pratt, P.A. Patel, T. Doel, S. Ourselin and T. Vercauteren are with Center for Medical Image Computing, University College London. R. Pratt and A.L. David are with Institute for Women's Health, University College London. M. Aertsen is with Department of Radiology, University Hospitals KU Leuven. J. Deprest is with Department of Obstetrics, University Hospitals KU Leuven. E-mail: guotai.wang.14@ucl.ac.uk

end utilizing the back-propagation algorithm. However, this CRF constrains the pairwise potentials as Gaussian functions which may be too constrained for some complex cases, and it does not apply automatic learning to all its parameters. Thus, using more freeform learnable pairwise potential functions and allowing automatic learning of all parameters can potentially achieve better results.

This paper aims to integrate user interactions into CNN frameworks to obtain accurate and robust segmentation of medical images, and at the same time, we aim to make the interactive framework more efficient with a minimal number of user interactions by using CNNs. With the good performance of CNNs shown for automatic image segmentation tasks [10], [11], [13], [14], [16], we hypothesize that they can reduce the number of user interactions in interactive image segmentation. However, only a few works have been reported to apply CNNs to interactive segmentation tasks [18], [19], [20], [21].

The contributions of this work are four-fold. 1), We propose a deep CNN-based interactive framework for medical image segmentation. We improve the CNN-based segmentation through integrating user interactions including clicks and scribbles. At the same time, the framework significantly reduces the amount of required interactions by using CNNs. We use one CNN to automatically get an initial segmentation, which is refined by another CNN that takes as input the initial segmentation and user interactions. 2), We present a new way to combine user interactions with CNNs based on geodesic distance maps. Geodesic distances of each pixel to user interactions of each class are calculated and they are used as extra channels of the input for CNNs. We show that using geodesic distance can lead to improved segmentation accuracy compared with Euclidean distance. 3), We propose a resolution-preserving CNN structure so that the image resolution is kept the same in all the convolutional layers. This can lead to a more detailed segmentation result compared with traditional CNNs with resolution loss. 4), We extend the current RNN-based CRFs [17] for segmentation so that the back-propagatable CRFs can use user interactions as hard constraints and all the parameters of its potential functions can be trainable in an end-to-end way. We apply the proposed method to segment the placenta from fetal MRI and the clavicle from chest radiographs.

2 RELATED WORK

2.1 Image Segmentation based on CNNs

Typical CNNs such as AlexNet [22], GoogleNet [23], VGG [24] and ResNet [25] were originally designed for image classification tasks. Some early works on CNN-based segmentation adapted such networks for pixel labeling with patch or region-based methods [10], [13]. For example, [26], [27] used a CNN to classify each pixel into the target object or the background by taking a local patch centered on that pixel as input. Such methods achieved higher accuracy than traditional methods that relied on hand-crafted features, but they suffered from inefficiency for testing.

Instead of using image patches, FCN [11] takes the entire image as input and outputs dense segmentation. In order to overcome the problem of reduction of spatial resolution due to multi-stage max-pooling and downsampling, it uses

a stack of deconvolution (a.k.a. upsampling) layers and activation functions to upsample the feature maps. Inspired by the convolution and deconvolution framework of FCN, a U-shape network (U-Net) [28] and its 3D version [18] were proposed for biomedical image segmentation. A similar network (V-Net) [29] was proposed to segment the prostate from 3D MRI volumes.

To avoid reduction of feature map resolution due to the successive max-pooling and downsampling while keeping an exponential growing of receptive field, dilated convolution [12] was proposed to replace the last two downsampling layers of the VGG network. The dilated convolution uses filters to sparsely sample the feature maps on which they are applied on using an input stride. It was used in [15] to preserve the resolution of feature maps and enlarge the receptive field to incorporate larger contextual information. In [30], a stack of dilated convolutions were used for object tracking and semantic segmentation. They have also been used by the instance-sensitive FCN [31] and applied to action segmentation and detection from video frames [32].

Multi-scale features extracted from CNNs have been shown to be effective for improving segmentation accuracy [11], [12], [15]. One way of obtaining multi-scale features is to pass several scaled versions of the input image through the same network. The features from all the scales can be fused for pixel classification [33]. In [13], [14], the features of each pixel were extracted from two cocentric patches with different sizes. In [34], multi-scale images at different stages were fed into a recurrent convolutional neural network. Another widely used way to obtain multi-scale features is exploiting features from different levels of the convolutional network. For example, in [35], features from intermediate layers are concatenated for segmentation and localization. In [11], [12], predictions from the final layer are combined with those from previous layers.

2.2 Interactive Image Segmentation

Interactive image segmentation has been widely used in various applications [20], [36], [37]. There are many kinds of user interactions, such as click-based [38], contour-based [4] and bounding box-based methods [7]. Drawing Scribbles is user-friendly and particularly popular, e.g., in Graph Cuts [3], GeoS [6], [39], and Random Walks [5]. However, most of these methods rely on low-level features and require a relatively large amount of user interactions to deal with images with low contrast and ambiguous boundaries. Machine learning methods [8], [40], [41] have been proposed to learn high-level features from user interactions. They can achieve higher segmentation accuracy with fewer user interactions. However, they are limited by hand-crafted features that depend on the user's experience.

Recently, using deep CNNs to improve interactive segmentation is attracting increasing attention due to CNNs' automatic feature learning and high performance. In [18], a 3D U-Net was proposed to learn from sparsely annotated data and can be used for semi-automatic segmentation. ScribbleSup [19] also trains CNNs for semantic segmentation supervised by scribbles. DeepCut [20] combines CNNs with user-provided bounding box annotations for image segmentation of fetal MRI. But these methods are not fully

interactive for testing since they do not accept further interactions for refinement. In [21], a deep interactive object selection method was proposed where user-provided clicks are transformed into Euclidean distance maps and then concatenated with the input of a FCN. However, the Euclidean distance does not take advantage of image context information. In contrast, geodesic distance transform [6], [39] encodes spatial regularization and contrast-sensitivity but it has not been used for CNNs.

2.3 CRFs for Spatial Regularization

Pixel-wise or super-pixel-wise classification based on CNNs or traditional classifiers often lacks spatial consistency. To overcome this problem, graphic models such as CRFs [12], [42], [43] have been widely used to enhance the accuracy of pixel labeling tasks. In [42], a discrete Potts model was proposed for spatial regularization where the Potts energy was minimized by a min-cut/max-flow algorithm. In [43], the discrete graph-based max-flow problem was mapped to its continuous optimization formulation that could be speeded up by parallel implementation on GPUs. Such methods encourage segmentation consistency between pixel pairs with high similarity. The pixel pairs are defined based on local neighborhoods or patches. In order to better model long-range connections within the image, a fully connected CRF was used in [44], [45] to establish pairwise potential on all pairs of pixels in the image with a Gaussian decay. The parameters of CRFs were manually tuned in these works. In [46], a maximum margin learning method was proposed to learn CRFs using Graph Cuts. Other methods including structured output Supporter Vector Machine [47] and approximate marginal inference [48] were also proposed to learn parameters in CRFs. They treat the learning of CRFs as an independent step after the training of classifiers.

The CRF-RNN network [17] formulated dense CRFs as RNNs so that the CNNs and CRFs can be jointly trained in an end-to-end system for segmentation. However, the pairwise potentials in [17] are limited to weighted Gaussians and not all the parameters are trainable due to the Permutohedral lattice implementation [49]. In [50], a Gaussian Mean Field (GMF) network was proposed and combined with CNNs where all the parameters are trainable. More freeform pairwise potentials for a pair of super-pixels or image patches were learned by neural networks [33], [51], but such CRFs have a low resolution. In [52], a generic CNN-CRF model was proposed to handle arbitrary potentials for labeling body parts in depth images, but it has not yet been validated for other segmentation applications.

3 METHOD

The proposed deep interactive geodesic distance-based segmentation method (DeepIGeoS) is depicted in Fig. 1. To minimize user interactions, we propose to use two CNNs: an initial segmentation proposal network (P-Net) and a refinement network (R-Net). The P-Net takes as input a raw image with C_I channels and automatically gives an initial segmentation. Then the user checks the segmentation and gives some interactions (clicks or scribbles) to indicate mis-segmented regions. The R-Net takes the information

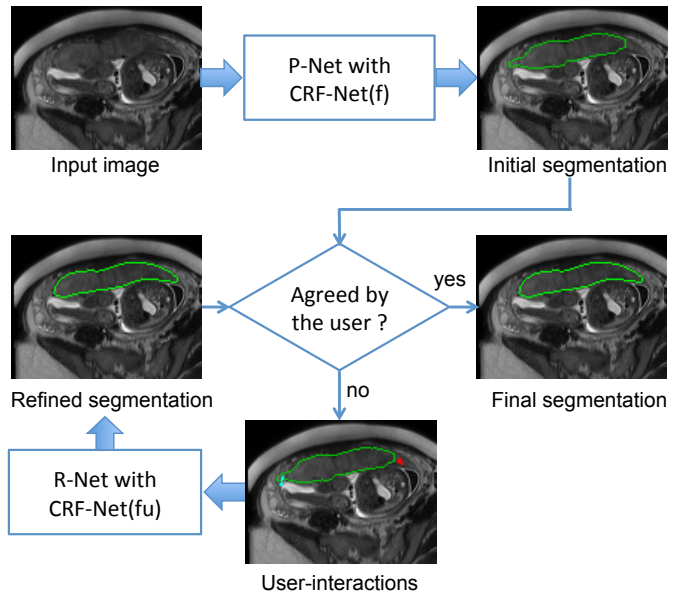


Fig. 1. Overview of the proposed interactive segmentation method. P-Net automatically proposes an initial segmentation which is refined by R-Net with user interactions indicating mis-segmentations. CRF-Net(f) is our proposed back-propagatable CRF that uses freeform pairwise potentials. It is extended to be CRF-Net(fu) that uses user interactions as hard constraints.

of the original input image, the initial segmentation and the user interactions to provide a refined segmentation. P-Net and R-Net use a resolution-preserving structure that captures high-level features from a large receptive field without loss of resolution. They share the same structure except the difference in the input dimensions. Based on the initial segmentation automatically obtained by P-Net, the user might give clicks/scribbles to refine the result more than one time through R-Net.

To make the segmentation result more spatially consistent and use scribbles as hard constraints, both P-Net and R-Net are connected with a CRF, which is modeled as an RNN (CRF-Net) so that it can be trained jointly with P-Net/R-Net by back-propagation. We use freeform pairwise potentials in the CRF-Net. The way user interactions are used is presented in 3.1. The structures of P-Net and R-Net are detailed in 3.2. In 3.3, we describe the implementation of our CRF-Net.

3.1 User Interaction-based Geodesic Distance Maps

In our method, a user checks an initial segmentation result that is automatically obtained by P-Net and gives scribbles (or clicks) to indicate mis-segmentation. A scribble gives a set of pixels the label of "foreground" or "background". Interactions with the same label are converted into a distance map. In [21], Euclidean distance was used due to its simplicity. However, the Euclidean distance treats each direction equally and does not take image context into account. In contrast, using geodesic distance helps to better differentiate neighboring pixels with different appearances, and improve label consistency in homogeneous regions [6]. GeoF [53] uses geodesic distance to encode variable dependencies in the feature space and it is combined with Random Forests

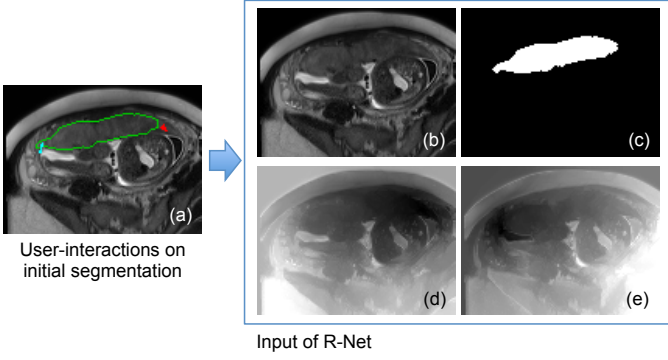


Fig. 2. Input of R-Net using geodesic distance transforms of user interactions. (a) The user gives clicks/scribbles to correct foreground (red) and background (cyan) on the initial segmentation. (d) and (e) are geodesic distance maps based on foreground and background interactions respectively. The original image intensity (b) is combined with the initial segmentation (c) and geodesic distance maps (d), (e) by channel-concatenation and used as the input of R-Net.

for semantic segmentation. However, it is not designed to deal with user interactions. We propose to encode user interactions via geodesic distance transform for CNN-based segmentation.

Supposing \mathcal{S}_f and \mathcal{S}_b represent the set of pixels belonging to foreground scribbles and background scribbles respectively. The unsigned geodesic distance from each pixel i in an image \mathbf{I} to the scribble set $\mathcal{S} (\mathcal{S} \in \{\mathcal{S}_f, \mathcal{S}_b\})$ is:

$$G(i, \mathcal{S}, \mathbf{I}) = \min_{j \in \mathcal{S}} D_{geo}(i, j, \mathbf{I}) \quad (1)$$

$$D_{geo}(i, j, \mathbf{I}) = \min_{p \in \mathcal{P}_{i,j}} \int_0^1 \|\nabla \mathbf{I}(p(s)) \cdot \mathbf{u}(s)\| ds \quad (2)$$

where $\mathcal{P}_{i,j}$ is the set of all paths between pixel i and j . p is one feasible path and it is parameterized by $s \in [0,1]$. $\mathbf{u}(s)$ is a unit vector which is tangent to the direction of the path and is defined as $\mathbf{u}(s) = p'(s)/\|p'(s)\|$. If no scribbles are drawn for the foreground or background, the corresponding geodesic distance map is filled with random numbers.

Fig. 2 shows an example of the geodesic distance transform of user interactions. The geodesic distance maps of user interactions and the original segmentation have the same height and width as \mathbf{I} , and they are concatenated with the channels of \mathbf{I} so that a concatenated image with C_I+3 channels is obtained and it is used as the input of the refinement network R-Net.

3.2 Resolution-Preserving CNN Structures using Dilated Convolution

The CNN structure in our method is designed to capture high-level features from a large receptive field without loss of resolution of feature maps. To simplify the comparison with existing network structures, our CNN structure is adapted from VGG-16 [24] and it is made resolution-preserving. There are 13 convolutional layers that are grouped into five blocks. Each of the first two blocks has two convolutional layers, and each of remaining blocks has three convolutional layers. The size of convolutional kernel is fixed as 3×3 in all these convolutional layers. Fig. 3

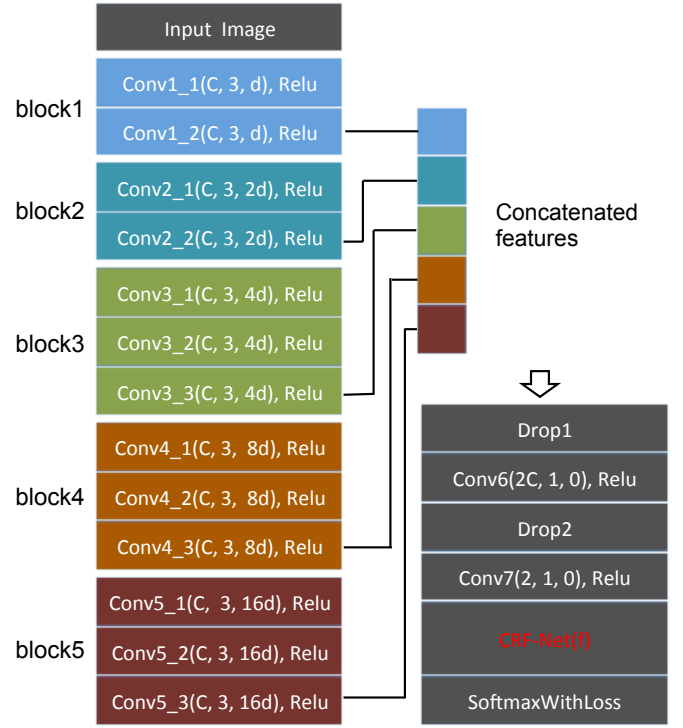


Fig. 3. The CNN structure of P-Net with CRF-Net(f). Parameters of a convolution layer are represented as $(C, 2r+1, q)$ where C is number of output channels, $2r+1$ is the convolutional kernel size and q is the dilation parameter as well as the padding size. The stride of each convolutional layer is set to 1 so that the resolution is kept the same through the network. R-Net uses the same structure except its input has three additional channels shown in Fig. 2 and the CRF-Net(f) is replaced by CRF-Net(fu) (Section 3.3).

shows the structure of P-Net. R-Net is the same except the difference in input channels and using user interactions in CRF-Net. To obtain an exponential increase of the receptive field, VGG-16 uses a max-pooling and downsampling layer after each block. However, this implementation would at the same time decrease the resolution of feature maps exponentially. Therefore, to preserve resolution through the network, we remove the max-pooling and downsampling layers and use dilated convolution in each block.

Let \mathbf{I} be a 2D image of size $W \times H$, and let K_{rq} be a square dilated convolutional kernel with a size of $(2r+1) \times (2r+1)$ and a dilation factor q , where $r \in \{0, 1, 2, \dots\}$ and $q \in \{0, 1, 2, \dots\}$. The dilated convolutional output of \mathbf{I} with K_{rq} is defined as:

$$\mathbf{I}_c(x, y) = \sum_{i=-r}^r \sum_{j=-r}^r \mathbf{I}(x - qi, y - qj) K_{rq}(i + r, j + r) \quad (3)$$

In our networks, for block 1 to block 5, we set r to 1 so the size of a convolutional kernel becomes 3×3 . The dilation factor in block i is set to:

$$q_i = d \times 2^{i-1}, i = 1, 2, \dots, 5 \quad (4)$$

where $d \in \{0, 1, 2, \dots\}$ is a system parameter controlling the base dilation factor of the network. We set $d=1$ in our experiments.

The receptive field of a dilated convolutional kernel K_{rq} is $(2rq+1) \times (2rq+1)$. Let $R_i \times R_i$ denote the receptive field of block i . R_i can be computed as:

$$R_i = 2 \left(\sum_{j=1}^i \tau_j \times (rq_j) \right) + 1, i = 1, 2, \dots, 5 \quad (5)$$

where τ_j is the number of convolutional layers in block j , with a value of 2, 2, 3, 3, 3 for the five blocks respectively. For $r=1$, the width of receptive field of each block is $R_1=4d+1$, $R_2=12d+1$, $R_3=36d+1$, $R_4=84d+1$, $R_5=180d+1$, respectively. Thus, these blocks capture features at different scales.

The stride of each convolutional layer is set to 1. The number of output channels of convolution in each block is set to a fixed number C . In order to use multi-scale features, we concatenate the features from different blocks to get a composed feature of length $5C$. This feature is fed into a classifier which is implemented by two additional layers Conv6 and Conv7 as shown in Fig. 3. Conv6 and Conv7 use convolutional kernels with size of 1×1 and dilation factor of 0, and the number of output channels for them is $2C$ and 2 respectively. Conv7 gives each pixel an initial score of belonging to the foreground or background class. In order to get a more spatially consistent segmentation and add hard constraints when scribbles are given, we apply a CRF on the basis of the output from Conv7. The CRF is implemented by a recurrent neural network (CRF-Net, detailed in 3.3) which can be jointly trained with P-Net or R-Net. The CRF-Net gives a regularized prediction for each pixel, which is fed into a cross entropy loss function layer.

3.3 Back-propagatable CRF-Net with Freeform Pairwise Potential and User Constraints

In [17] a CRF based on RNN was proposed and it was trainable by back-propagation. Rather than using Gaussian functions, we extend this CRF so that the pairwise potential can be freeform functions and refer to it as CRF-Net(f). In addition, we integrate user interactions in our CRF-Net(f) in the interactive refinement context, which is referred to as CRF-Net(fu). CRF-Net(f) is connected to P-Net and CRF-Net(fu) is connected to R-Net.

Let \mathbf{X} be the label map assigned to an image \mathbf{I} with a label set $\mathcal{L} = \{0, 1, \dots, L\}$. The Gibbs distribution $P(\mathbf{X} = \mathbf{x} | \mathbf{I}) = \frac{1}{Z(\mathbf{I})} \exp(-E(\mathbf{x} | \mathbf{I}))$ models the probability of \mathbf{X} given \mathbf{I} in a CRF, where $Z(\mathbf{I})$ is the normalization factor known as the partition function, and $E(\mathbf{x})$ is the Gibbs energy:

$$E(\mathbf{x}) = \sum_i \psi_u(x_i) + \sum_{(i,j) \in \mathcal{N}} \psi_p(x_i, x_j) \quad (6)$$

where the unary potential $\psi_u(x_i)$ measures the cost of assigning label x_i to pixel i , and the pairwise potential $\psi_p(x_i, x_j)$ is the cost of assigning labels x_i, x_j to pixel pair i, j . \mathcal{N} is the set of all pixel pairs. In our method, the unary potential is obtained from P-Net or R-Net which gives initial classification scores at each pixel. The pairwise potential is:

$$\psi_p(x_i, x_j) = \mu(l_i, l_j) f(\tilde{\mathbf{f}}_{ij}, d_{ij}) \quad (7)$$

where d_{ij} is the Euclidean distance between pixel i and j . $\mu(l_i, l_j)$ is the compatibility between the label of i and that of j represented by a matrix of size $L \times L$. $\tilde{\mathbf{f}}_{ij} = \mathbf{f}_i - \mathbf{f}_j$,

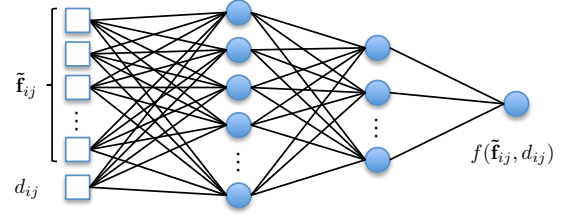


Fig. 4. The Pairwise-Net for pairwise potential function $f(\tilde{\mathbf{f}}_{ij}, d_{ij})$. $\tilde{\mathbf{f}}_{ij}$ is the difference of features between a pixel pair i and j . d_{ij} is the Euclidean distance between them.

and \mathbf{f}_i and \mathbf{f}_j represent the feature vectors of pixel i and j respectively. The feature vectors can either be learned by a network or be derived from image features such as spatial location with intensity values. For experiments we used the latter one, as used in [3], [17], [45] for simplicity and efficiency. $f(\cdot)$ is a function in terms of $\tilde{\mathbf{f}}_{ij}$ and d_{ij} . Instead of defining $f(\cdot)$ as a single Gaussian function [3] or a combination of several Gaussian functions [17], [45], we set it as a freeform function represented by a fully connected neural network (Pairwise-Net) which can be learned during training. The structure of Pairwise-Net is shown in Fig. 4. The input is a vector composed of $\tilde{\mathbf{f}}_{ij}$ and d_{ij} . There are two hidden layers and one output layer.

Graph Cuts [3], [46] can be used to minimize Eq. (6) when $\psi_p(\cdot)$ is submodular [54] such as when the segmentation is binary with $\mu(\cdot)$ being the delta function and $f(\cdot)$ being positive. However, this is not the case for us since we learn $\mu(\cdot)$ and $f(\cdot)$ so that $\mu(\cdot)$ may not be the delta function and $f(\cdot)$ could be negative. Continuous max-flow [43] can also be used for the minimization, but its parameters are manually designed. Alternatively, mean-field approximation [17], [45], [50] is often used to efficiently minimize the energy while allowing learning parameters by back-propagation. Instead of computing $P(\mathbf{X} | \mathbf{I})$ directly, an approximate distribution $Q(\mathbf{X} | \mathbf{I}) = \prod_i Q_i(x_i | \mathbf{I})$ is computed so that the KL-divergence $\mathbf{D}(Q || P)$ is minimized. This yields an iterative update of $Q_i(x_i | \mathbf{I})$ [17], [45], [50].

$$Q_i(x_i | \mathbf{I}) = \frac{1}{Z_i} e^{-E(x_i)} = \frac{1}{Z_i} e^{-\psi_u(x_i) - \phi_p(x_i)} \quad (8)$$

$$\phi_p(x_i = l | \mathbf{I}) = \sum_{l' \in \mathcal{L}} \mu(l, l') \sum_{(i,j) \in \mathcal{N}} f(\tilde{\mathbf{f}}_{ij}, d_{ij}) Q_j(l' | \mathbf{I}) \quad (9)$$

where \mathcal{L} is the label set. i and j are a pixel pair. For the proposed CRF-Net(fu), with the set of user-provided scribbles $\mathcal{S}_{fb} = \mathcal{S}_f \cup \mathcal{S}_b$, we force the probability of pixels in the scribble set to be 1 or 0. The following equation is used as the update rule for each iteration:

$$Q_i(x_i | \mathbf{I}) = \begin{cases} 1 & \text{if } i \in \mathcal{S}_{fb} \text{ and } x_i = s_i \\ 0 & \text{if } i \in \mathcal{S}_{fb} \text{ and } x_i \neq s_i \\ \frac{1}{Z_i} e^{-E(x_i)} & \text{otherwise} \end{cases} \quad (10)$$

where s_i denotes the user-provided label of a pixel i that is in the scribble set \mathcal{S}_{fb} . We follow the implementation in [17] to update Q through a multi-stage mean-field method in an RNN. Each mean-field layer splits Eq. (8) into four steps including message passing, compatibility transform, adding unary potentials and normalizing [17].

3.4 Implementation Details

Computation of geodesic distances follows the raster-scan algorithm proposed in [6] which is fast due to accessing the image memory in contiguous blocks. This method calculates the geodesic distance by applying a forward pass scanning and a backward pass scanning with a 3×3 kernel. For the proposed CRF-Net with freeform pairwise potentials, two observations motivate us to use pixel connections based on local patches instead of full connections within the entire image. First, the permutohedral lattice implementation [17], [45] allows efficient computation of fully connected CRFs only when pairwise potentials are Gaussian functions. However, a method that relaxes the requirement of pairwise potentials as freeform functions represented by a network (Fig. 4) cannot use that implementation and therefore would be inefficient for fully connected CRFs. Supposing an image with size $M \times N$, a fully connected CRF has $MN(MN-1)$ pixel pairs. For a small image with $M=N=100$, the number of pixel pairs would be almost 10^8 , which requires not only a huge amount of memory but also long computational time. Second, though long-distance dependency helps to improve segmentation in general RGB images [12], [17], [45], this would be very challenging for medical images since the contrast between the target and background is often low [55]. In such cases, long-distance dependency may lead the label of a target pixel to be corrupted by the large amount of background pixels with similar appearances. Therefore, to maintain a good efficiency and avoid long-distance corruptions, we define the pairwise connections for one pixel within a local patch centered on that. In our experiment, the patch size is set to 7×7 based on experience.

We initialize $\mu(\cdot)$ as $\mu(l_i, l_j) = [l_i \neq l_j]$, where $[\cdot]$ is the Iverson Bracket. A fully connected neural network (Pairwise-Net) with two hidden layers is used to learn the freeform pairwise potential function (Fig. 4). The first and second hidden layer have 32 and 16 neurons respectively. In practice this network is implemented by an equivalent fully convolutional neural network. We use a pre-training step to initialize the Pairwise-Net with an approximation of a contrast sensitive function as described in the following [3]:

$$f_0(\tilde{\mathbf{f}}_{ij}, d_{ij}) = \exp\left(-\frac{\|\tilde{\mathbf{f}}_{ij}\|^2}{2\sigma^2 \cdot F}\right) \cdot \frac{\omega}{d_{ij}} \quad (11)$$

where F is the dimension of feature vector \mathbf{f}_i and \mathbf{f}_j , and ω and σ are two parameters controlling the magnitude and shape of the initial pairwise function respectively. We set σ to 0.08 and ω to 0.5 based on experience. Similar to [16], [17], [45], we set \mathbf{f}_i and \mathbf{f}_j as values in input channels (i.e. image intensity in our case) of P-Net for simplicity as well as obtaining contrast-sensitive pairwise potentials. To pre-train Pairwise-Net we generate a training set $T' = \{X', Y'\}$ of 100k samples, where X' is the set of features simulating the concatenated $\tilde{\mathbf{f}}_{ij}$ and d_{ij} , and Y' is the set of prediction values simulating $f_0(\tilde{\mathbf{f}}_{ij}, d_{ij})$. For each sample s in T' , the feature vector x'_s has a dimension of $F+1$ where the first F dimensions represent the value of $\tilde{\mathbf{f}}_{ij}$ and the last dimension denotes d_{ij} . The c -th channel of x'_s is filled with a random number k' , where $k' \sim \text{Norm}(0, 2)$ for $c \leq F$ and $k' \sim U(0, 8)$ for $c = F+1$. The ground truth of prediction value y'_s for x'_s is obtained by Eq. (11). After generating X' and Y' , we

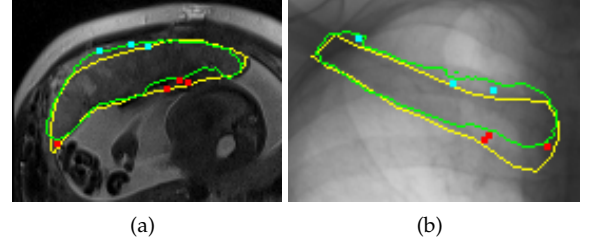


Fig. 5. Examples of simulated user interactions on training slices for placenta in fetal MRI (a) and clavicle in chest radiographs (b). Green: automatic segmentation given by P-Net with CRF-Net(f). Yellow: ground truth. Red(cyan): simulated clicks on under-segmentation(over-segmentation).

use a Stochastic Gradient Descent (SGD) algorithm with a quadratic loss function to pre-train the Pairwise-Net.

As a pre-processing step, the image data are normalized by the mean value and standard variation of training images. We apply data augmentation by vertical or horizontal flipping, random rotation with angle range $[-\pi/8, \pi/8]$ and random zoom with scaling factor range $[0.8, 1.25]$. We use the cross entropy loss function and SGD algorithm for optimization with minibatch size 1, momentum 0.99 and weight decay 5×10^{-4} . The learning rate is halved every 5k iterations. Since a proper initialization of P-Net and CRF-Net(f) is helpful for a faster convergence of the joint training, we train the P-Net with CRF-Net(f) in three steps. First, P-Net is pre-trained with initial learning rate 10^{-3} and maximal number of iterations 100k. Second, For CRF-Net(f), the Pairwise-Net is pre-trained as described above. Third, P-Net and CRF-Net(f) are jointly trained with initial learning rate 10^{-6} and maximal number of iterations 50k.

After training of P-Net with CRF-Net(f), we automatically simulate user interactions to train R-Net with CRF-Net(fu). First, P-Net with CRF-Net(f) is used to obtain an automatic segmentation for each training image. It is compared with the ground truth to find mis-segmented regions. Then the user interactions on each mis-segmented region are simulated by randomly sampling N_c pixels in that region. Supposing the size of one connected under-segmented or over-segmented region is N_m , we set N_c for that region to 0 if $N_m < 30$ and $\lceil N_m/100 \rceil$ otherwise based on experience. Examples of simulated user interactions on training images are shown in Fig. 5. With these simulated user interactions on the initial segmentation of training data, the R-Net with CRF-Net(fu) is subsequently trained in three steps as used by P-Net with CRF-Net(f).

We used the Caffe¹ [56] deep learning library to implement the proposed P-Net and R-Net with CRF-Net. Our training process was done via two 8-core E5-2623v3 Intel Haswells and two K80 NVIDIA GPUs and 128GB memory. The testing process with user interactions was performed on a MacBook Pro (OS X 10.9.5) with 16GB RAM and an Intel Core i7 CPU running at 2.5GHz and an NVIDIA GeForce GT 750M GPU. A Matlab GUI was developed for user interactions.

1. <http://caffe.berkeleyvision.org>

4 EXPERIMENTS

4.1 Comparison Methods and Evaluation Metrics

To evaluate the performance of our network structures, we compared our P-Net with FCN [11] and DeepLab [16]. Pre-trained models of FCN² and DeepLab³ based on ImageNet were fine-tuned for our segmentation tasks. These two networks were extensions from VGG-16 [24] so that they allow obtaining the label of an image through one single forward pass. However, the output resolution of these two networks was 1/8 of the input resolution, therefore the output was upsampled to obtain the final result. For fine-tuning, we used the same learning rate schedules as those used for training P-Net. The maximal number of iterations was set to 100k. Since the input of FCN and DeepLab should have three channels, we duplicated each of the gray-level images twice and composed them into a 3-channel image as the input. We also compared P-Net with its variation P-Net(b5) that only uses features from block 5 (Fig. 3) instead of concatenated multi-scale features.

The proposed CRF-Net(f) was compared with two counterparts: 1), CRF-Post which refers to using CRFs as an independent post processing step for the output of P-Net. We followed the implementation presented in [16], [45]. Instead of being learned by back-propagation, the parameters of this CRF were manually tuned based on a coarse-to-fine search scheme as suggested by [16]; 2), CRF-Net(g) which refers to the CRF proposed in [17] that can be trained jointly with CNNs by using Gaussian functions as pairwise potentials.

To evaluate the performance of DeepGeoS, we compared it with four other interactive segmentation methods: 1), GeoS [6] that computes a probability based on the geodesic distance from user-provided scribbles for pixel classification; 2), Graph Cuts [3] that models segmentation as a min-cut problem based on user interactions; 3), Random Walks [5] that assigns a pixel with a label based on the probability that a random walker reaches a foreground seed first; 4), SlicSeg [8] that uses Online Random Forests to learn from scribbles and predict remaining pixels. Two users (an Obstetrician and a Radiologist) respectively used these segmentation methods to segment every test image until the result was visually acceptable.

For quantitative evaluation, we measured the Dice score and the average symmetric surface distance (ASSD).

$$\text{Dice} = \frac{2|\mathcal{R}_a \cap \mathcal{R}_b|}{|\mathcal{R}_a| + |\mathcal{R}_b|} \quad (12)$$

where \mathcal{R}_a and \mathcal{R}_b represent the region segmented by the algorithms and the ground truth, respectively.

$$\text{ASSD} = \frac{1}{|\mathcal{S}_a| + |\mathcal{S}_b|} \left(\sum_{i \in \mathcal{S}_a} d(i, \mathcal{S}_b) + \sum_{i \in \mathcal{S}_b} d(i, \mathcal{S}_a) \right) \quad (13)$$

where \mathcal{S}_a and \mathcal{S}_b represent the set of surface points of the target segmented by algorithms and the ground truth respectively. $d(i, \mathcal{S}_b)$ is the shortest Euclidean distance between i and \mathcal{S}_b . We used the Student's t -test to compute the p -value in order to see whether the results of two algorithms significantly differ from each other.

2. <https://github.com/shelhamer/fcn.berkeleyvision.org>
 3. <https://bitbucket.org/deeplab/deeplab-public>

TABLE 1

Quantitative comparison of placenta segmentation by different networks and CRFs. CRF-Net(g) [17] constrains pairwise potential as Gaussian functions. CRF-Net(f) is our proposed CRF that learns freeform pairwise potential functions. Significant improvement from P-Net (p -value < 0.05) is shown in bold font.

Method	Dice(%)	ASSD(pixels)
FCN	81.47±11.40	2.66±1.39
DeepLab	83.38±9.53	2.20±0.84
P-Net(b5)	83.16±13.01	2.36±1.66
P-Net	84.78±11.74	2.09±1.53
P-Net + CRF-Post	84.90±12.05	2.05±1.59
P-Net + CRF-Net(g)	85.44±12.50	1.98±1.46
P-Net + CRF-Net(f)	85.86±11.67	1.85±1.30

4.2 Segmentation of the Placenta from Fetal MRI

4.2.1 Clinical Background and Experiments Setting

Fetal MRI is an emerging diagnostic tool complementary to ultrasound due to its large field of view and good soft tissue contrast. Segmenting the placenta from fetal MRI is important for fetal surgical planning, e.g., in the case of twin-to-twin transfusion syndrome [57]. Clinical fetal MRI data are often acquired with a large slice thickness for good contrast-to-noise ratio. Movement of the fetus can lead to inhomogeneous appearances between slices. In addition, the location and orientation of the placenta vary largely between individuals. These factors make automatic and 3D segmentation of the placenta a challenging task [58]. Interactive 2D slice-based segmentation is expected to achieve more robust results [8], [59]. The 2D segmentation results can also be used for motion correction and high-resolution volume reconstruction [60].

We collected clinical MRI scans for 25 pregnancies in the second trimester. The data were acquired in axial view with pixel size between 0.7422 mm×0.7422 mm and 1.582 mm×1.582 mm and slice thickness 3 - 4 mm. Each slice was resampled with a uniform pixel size of 1 mm×1 mm and cropped by a box of size 172×128 containing the placenta. We used 17 volumes with 624 slices for training, three volumes with 122 slices for validation and five volumes with 179 slices for testing. The ground truth was manually delineated by two experienced Radiologists.

4.2.2 Automatic Segmentation by P-Net with CRF-Net(f)

Fig. 6 shows the automatic segmentation results obtained by different network structures. It shows that FCN is able to capture the main region of the placenta. However, the segmented regions are blob-like with smooth boundaries. DeepLab is better than FCN, but its blob-like results are similar to those of FCN. This is mainly due to the downsampling and upsampling procedure employed by these methods. In contrast, P-Net(b5) and P-Net obtain more detailed results with less smooth boundaries. It can be observed that P-Net achieves better results than the other three networks. However, there are still some obvious mis-segmented regions by P-Net. Quantitative comparison of these network structures based on all the testing data is shown in Table 1. P-Net achieves a Dice score of 84.78±11.74% and an ASSD of 2.09±1.53 pixels and it performs better than other three network structures.

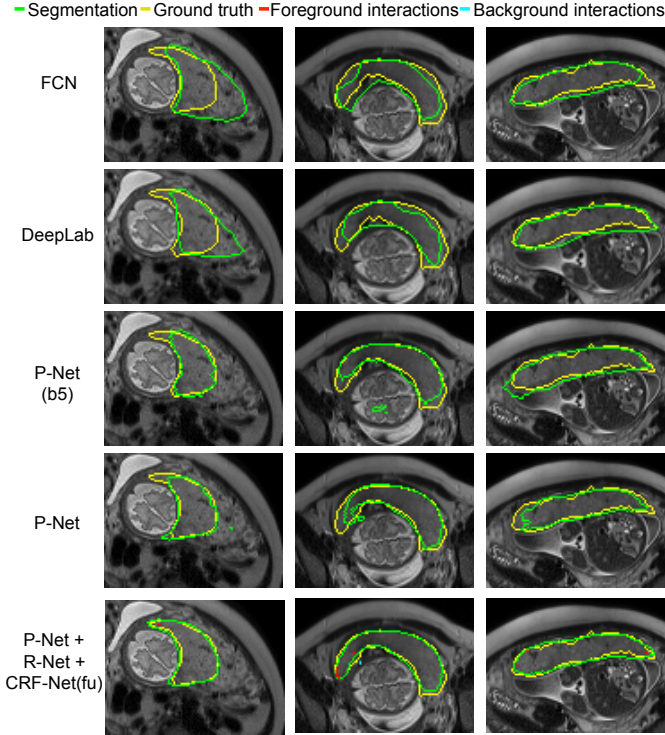


Fig. 6. Initial automatic segmentation results of the placenta by P-Net. P-Net(b5) only uses the features from block 5 shown in Fig. 1 rather than the concatenated multi-scale features. Notice the more accurate and detailed segmentation results of P-Net compared with FCN [11] and DeepLab [16]. The last row shows user interactions and refined segmentation.

Based on P-Net, we investigated the performance of different CRFs. A visual comparison between CRF-Post, CRF-Net(g) and CRF-Net(f) is shown in Fig. 7. In the first column, the placenta is under-segmented by P-Net. CRF-Post leads to very small improvements on the result. CRF-Net(g) and CRF-Net(f) improve the result by preserving more placenta regions, and the later shows a better segmentation. In the second column, P-Net obtains an over-segmentation of adjacent fetal brain and maternal tissues. CRF-Post does not improve the segmentation noticeably, but CRF-Net(g) and CRF-Net(f) remove more over-segmentated areas. CRF-Net(f) shows a better performance than the other two CRFs. The quantitative evaluation of these three CRFs is presented in Table 1, which shows CRF-Post leads to a result that is very close to that of P-Net (p -value > 0.05), while the last two CRFs significantly improve the segmentation (p -value < 0.05). In addition, CRF-Net(f) is better than CRF-Net(g). Though using CRF-Net(f) leads to better segmentation, both Fig. 7 and Table 1 indicate that large mis-segmentation exists in some images, thus we use R-Net with CRF-Net(fu) to refine the segmentation interactively in the following.

4.2.3 Interactive Refinement by R-Net with CRF-Net(fu)

Fig. 8 shows examples of interactive refinement using R-Net with CRF-Net(fu). The first column in Fig. 8 shows initial segmentation results obtained by P-Net + CRF-Net(f). The user gives clicks/scribbles to indicate the foreground (red) or the background (cyan). The second to fifth column in Fig. 8 show the results for four variations of refinement

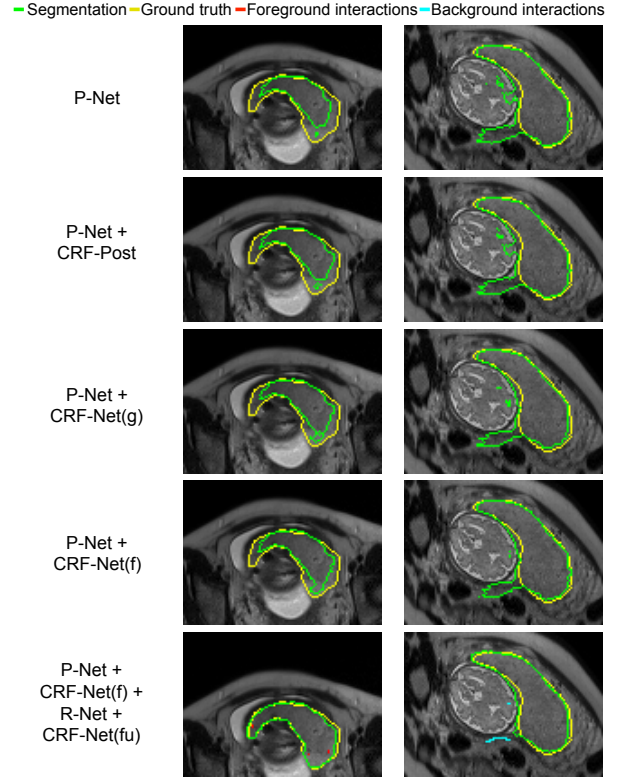


Fig. 7. Visual comparison of placenta segmentation by P-Net with different CRFs. The last row shows refinement by user interactions.

TABLE 2

Quantitative evaluation of placenta segmentation by R-Net with CRF-Net(fu) after the first iteration of refinement. The input is from the segmentation obtained by P-Net + CRF-Net(f). R-Net(Euc) uses Euclidean distance instead of geodesic distance. Significant improvement from R-Net (p -value < 0.05) is shown in bold font.

Method	Dice(%)	ASSD(pixels)
P-Net + CRF-Net(f)	85.86±11.67	1.85±1.30
R-Net(Euc)	88.26±10.61	1.54±1.18
R-Net	88.76±5.56	1.31±0.60
R-Net(Euc) + CRF-Net(fu)	88.71±8.42	1.26±0.59
R-Net + CRF-Net(fu)	89.31±5.33	1.22±0.55

based on R-Net using geodesic or Euclidean distance transforms with or without CRF-Net(fu). These four variations correct most of the mis-segmented areas but perform at different levels in dealing with local details, as indicated by white arrows. Fig. 8 shows geodesic distance performs better than Euclidean distance, and both of them achieve higher accuracy by working with CRF-Net(fu). For quantitative comparison, we measured the segmentation accuracy after the first iteration of user refinement (giving user interactions to mark all the main mis-segmented regions and applying R-Net once), in which the same initial segmentation and the same set of user interactions were used for the four variations of refinement. The results are presented in Table 2, which shows the combination of the proposed R-Net using geodesic distance and CRF-Net(fu) leads to more accurate segmentation than other variations with the same set of user interactions. The Dice score and ASSD of R-Net + CRF-Net(fu) are 89.31±5.33% and 1.22±0.55 pixels, respectively.

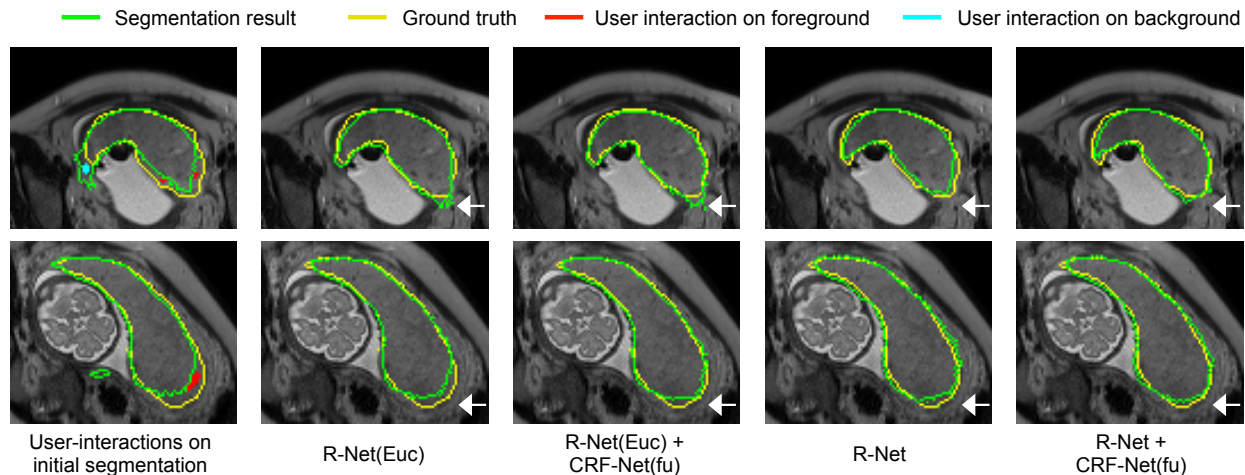


Fig. 8. Refinement of placenta segmentation by R-Net with CRF-Net(fu). The first column shows the initial segmentation obtained by P-Net + CRF-Net(f), on which user interactions are added for refinement. The remaining columns show refined results. R-Net(Euc) is a counterpart of the proposed R-Net and uses Euclidean distance. White arrows show the difference in local details.

4.2.4 Comparison with Other Interactive Methods

Fig. 9 shows a visual comparison between DeepIGeoS and GeoS [6], Graph Cuts [3], Random Walks [5] and SlicSeg [8] for placenta segmentation. The first row shows the initial scribbles and the resulting segmentation. Notice no initial scribbles are needed for DeepIGeoS. The second row shows the final results based on refinement, where DeepIGeoS only needs two short strokes to get an accurate segmentation, while other methods additionally require more scribbles to get similar results. Quantitative comparison of these methods based on the final segmentation given by two users is presented in Fig. 10. It shows different interactive methods achieve similar accuracy, but DeepIGeoS requires far fewer user interactions and less time.

4.3 Segmentation of the Clavicle from Radiographs

4.3.1 Clinical Background and Experiments Setting

Chest radiographs are widely used for the detection and diagnosis of lung diseases such as lung cancer. Some findings on chest radiographs such as sharply circumscribed nodules or masses can indicate the presence of lung cancer. However, due to superimposition of multiple structures including ribs and clavicles, lung nodule detection and analysis is challenging. Segmenting the bone structures from chest radiographs can help to digitally suppress bones thus increase the visibility of nodules [61]. In particular, clavicle suppression might aid radiologists in detecting pathologies in the lung apex for certain lung diseases such as tuberculosis. Thus, accurate clavicle segmentation is needed to improve pathology detection. This task is challenging due to low contrast and inhomogeneous appearance in the clavicle region resulting from superimposition of several structures. In [62], it was shown that segmenting the clavicle is more difficult than segmenting the heart and the lungs. In [63], pixel classification was combined with an active shape model for automatic clavicle segmentation, while the result showed large mis-segmented areas in some images.

TABLE 3

Quantitative comparison of clavicle segmentation by different networks and CRFs. Significant improvement from P-Net (p -value < 0.05) is shown in bold font.

Method	Dice(%)	ASSD(pixels)
FCN	81.08±13.73	3.38±2.31
DeepLab	82.27±10.80	3.09±1.47
P-Net(b5)	82.15±11.08	3.21±1.91
P-Net	84.18±10.94	2.79±1.78
P-Net + CRF-Post	83.52±11.69	2.84±1.86
P-Net + CRF-Net(g)	84.51±10.45	2.72±1.57
P-Net + CRF-Net(f)	84.83±10.52	2.65±1.52

We used the publicly available JSRT database⁴ which consists of 247 radiographs with image resolution 2048×2048 and pixel size 0.175 mm×0.175 mm. Ground truth of 93 images was given by the SCR database⁵ based on manual segmentation by an expert. The ground truth delineated the part of clavicle projected over the lungs and mediastinum. Data in the SCR database had been split into two groups with 47 and 46 images respectively. For the first group, we used 40 images as training data and the other 7 images as validation data. All the images in the second group were used as testing data. We downsampled each original image into a size of 512×512 pixels and manually cropped it with two 200×160 boxes covering the left and right clavicle respectively.

4.3.2 Automatic Segmentation by P-Net with CRF-Net(f)

Fig. 11 shows examples of automatic segmentation of the clavicle by P-Net, which is compared with FCN, DeepLab and P-Net(b5). In the first case, FCN segments the clavicle roughly, with some missed regions near the boundary. DeepLab reduces the missed regions but leads to some over-segmentation. P-Net(b5) obtains a similar result to that of DeepLab. In contrast, P-Net achieves a more accurate

4. <http://www.jsrt.or.jp/jsrt-db/eng.php>

5. <http://www.isi.uu.nl/Research/Databases/SCR/>

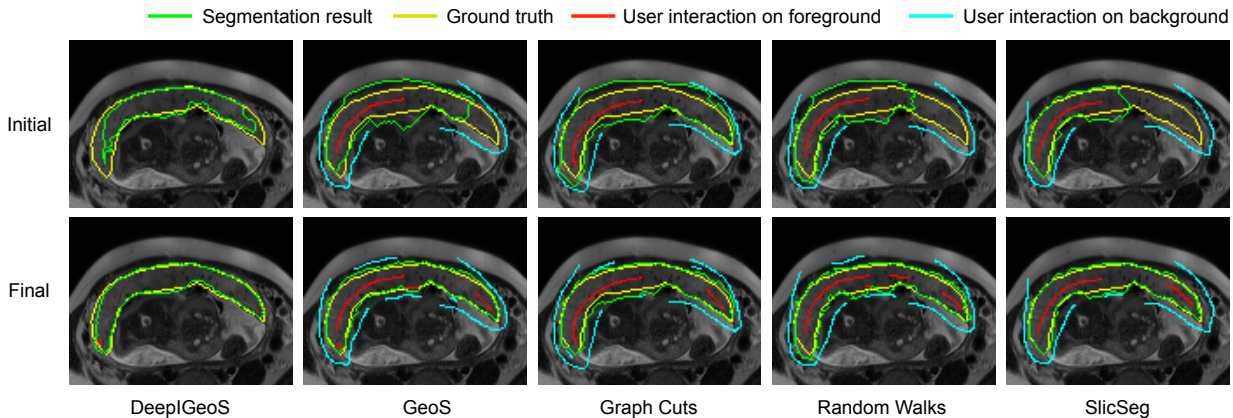


Fig. 9. Visual comparison of DeeplGeoS and other interactive methods for placenta segmentation. The first row shows initial scribbles (except for DeeplGeoS) and the resulting segmentation. The second row shows final refined results with the entire set of scribbles. The user decided on the level of interaction required to achieve a visually acceptable result.

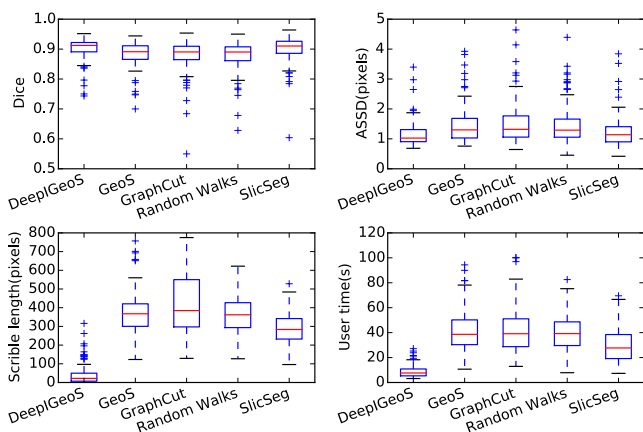


Fig. 10. Quantitative comparison of placenta segmentation by different interactive methods in terms of Dice, ASSD, total interactions (scribble length) and the user's time.

segmentation which is closer to the ground truth. In the second case, FCN only captures a small region of the clavicle, while DeepLab captures a larger region with both under-segmentation and over-segmentation. P-Net(b5) and P-Net obtain better results compared with FCN and DeepLab. Quantitative evaluation of these four networks is presented in Table 3. The result shows FCN has the worst performance. P-Net achieves the most accurate segmentation compared with other three networks. It achieves $84.18 \pm 10.94\%$ in terms of Dice and 2.79 ± 1.78 pixels in terms of ASSD.

The effect of different types of CRFs working with P-Net is shown in Fig. 12. It can be observed that CRF-Net(f) improves the segmentation better than CRF-Post and CRF-Net(g). Quantitative measurement of different CRFs is listed in Table 3. The result shows only CRF-Net(f) obtains significantly better segmentation than P-Net (p -value < 0.05).

4.3.3 Interactive Refinement by R-Net with CRF-Net(fu)

Fig. 13 shows examples of interactive refinement of clavicle segmentation using R-Net with CRF-Net(fu). The initial segmentation is obtained by P-Net + CRF-Net(f) and user interactions are given to indicate mis-segmented areas (first

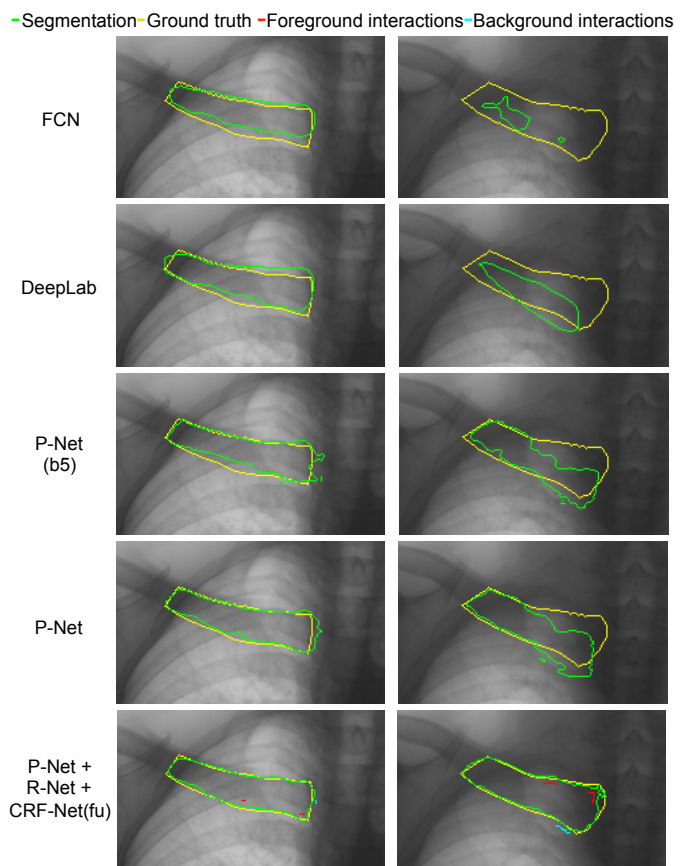


Fig. 11. Initial automatic segmentation results of the clavicle by different networks. The last row shows refinement by user interactions.

column). With the same set of user interactions, we compared the refined results of four variations of refinement based on R-Net using geodesic or Euclidean distance transforms with or without CRF-Net(fu). Fig. 13 shows that the segmentation is largely improved by refinements. The white arrows show the local difference between these four variations. It can be found that more accurate results are obtained by using geodesic distance than using Euclidean distance, and CRF-Net(fu) can further help to improve the

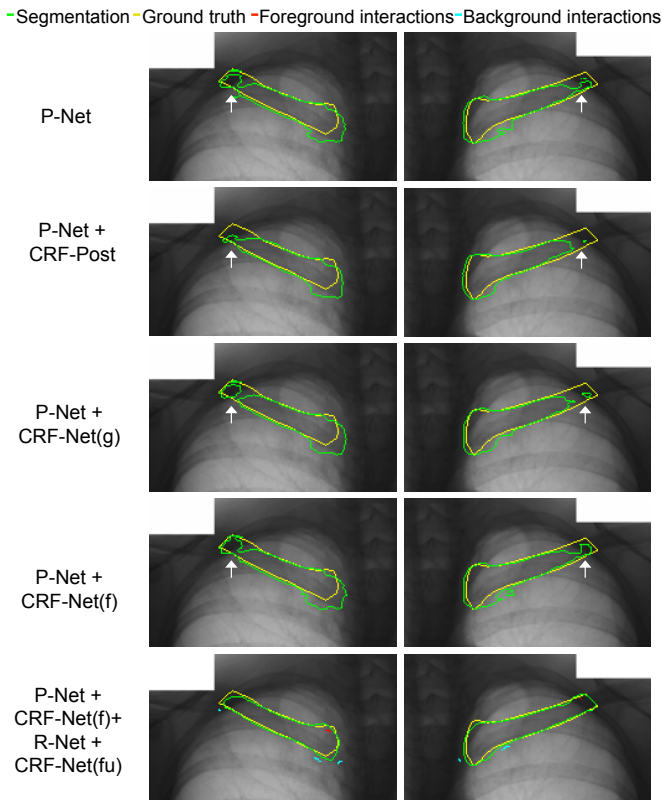


Fig. 12. Visual comparison of clavicle segmentation by P-Net with different CRFs. The last row shows refinement by user interactions.

TABLE 4

Quantitative evaluation of clavicle segmentation by R-Net with CRF-Net(fu) after the first iteration of refinement. The input is from the segmentation obtained by P-Net + CRF-Net(f). R-Net(Euc) uses Euclidean distance instead of geodesic distance. Significant improvement from R-Net (p -value < 0.05) is shown in bold font.

Method	Dice(%)	ASSD(pixels)
P-Net + CRF-Net(f)	84.83±10.52	2.65±1.52
R-Net(Euc)	88.34±8.91	2.20±2.17
R-Net	89.33±7.85	1.86±1.02
R-Net(Euc) + CRF-Net(fu)	88.83±8.32	1.96±1.09
R-Net + CRF-Net(fu)	90.22±6.41	1.73±0.87

segmentation. For quantitative comparison, we measured the segmentation accuracy after the first iteration of user refinement (applying R-Net once) using these methods with the same set of scribbles. The quantitative evaluation is listed in Table 4, showing that the proposed R-Net with geodesic distance and CRF-Net(fu) achieves higher accuracy than other variations with a Dice score of 90.22±6.41% and ASSD of 1.73±0.87 pixels.

4.3.4 Comparison with Other Interactive Methods

Fig. 14 compares DeepIGeoS and GeoS [6], Graph Cuts [3], Random Walks [5] and SlicSeg [8] for clavicle segmentation. The initial automatic segmentation by DeepGeoS has some errors at the head of the clavicle, and it is refined by only two short strokes given by the user. In contrast, other interactive methods rely on a large amount of interactions for initial segmentation, and the additional scribbles given for refinement are also long. Quantitative comparison between these

methods based on the results given by two users is shown in Fig. 15. Compared with traditional interactive methods, DeepIGeoS achieves similar Dice and ASSD values, but with far fewer scribbles and less time.

5 CONCLUSION

In this work, we presented a deep learning-based interactive framework for medical image segmentation. We proposed a P-Net to obtain an initial automatic segmentation and an R-Net to refine the result based on user interactions that are transformed into geodesic distance maps and then integrated into the R-Net’s input. We also proposed a resolution-preserving network structure with dilated convolution for dense prediction, and extended the existing RNN-based CRF so that it can learn freeform pairwise potentials and take advantage of user interactions as hard constraints. Segmentation results of the placenta from fetal MRI and the clavicle from chest radiographs show that our proposed method achieves better results than automatic CNNs, and it obtains similar accuracy with fewer user interactions and less time compared with traditional interactive methods. The framework can be extended to deal with 3D images and multiple organs in the future.

ACKNOWLEDGMENTS

This work was supported through an Innovative Engineering for Health award by the Wellcome Trust (WT101957); Engineering and Physical Sciences Research Council (EPSRC) (NS/A000027/1, EP/H046410/1, EP/J020990/1, EP/K005278), the National Institute for Health Research University College London Hospitals Biomedical Research Centre (NIHR BRC UCLH/UCL High Impact Initiative), NIHR BRC funding (AL David), a UCL Overseas Research Scholarship and a UCL Graduate Research Scholarship. The authors would like to acknowledge that the work presented here made use of Emerald, a GPU-accelerated High Performance Computer, made available by the Science & Engineering South Consortium operated in partnership with the STFC Rutherford-Appleton Laboratory.

REFERENCES

- [1] N. Sharma and L. M. Aggarwal, “Automated medical image segmentation techniques.” *Journal of medical physics*, vol. 35, no. 1, pp. 3–14, 2010.
- [2] F. Zhao and X. Xie, “An Overview of Interactive Medical Image Segmentation,” *Annals of the BMVA*, vol. 2013, no. 7, pp. 1–22, 2013.
- [3] Y. Boykov and M.-P. Jolly, “Interactive Graph Cuts for Optimal Boundary & Region Segmentation of Objects in N-D Images,” in *ICCV*, 2001, pp. 105–112.
- [4] C. Xu and J. L. Prince, “Snakes, Shapes, and Gradient Vector Flow,” *TIP*, vol. 7, no. 3, pp. 359–369, 1998.
- [5] L. Grady, “Random walks for image segmentation,” *PAMI*, vol. 28, no. 11, pp. 1768–1783, 2006.
- [6] A. Criminisi, T. Sharp, and A. Blake, “GeoS: Geodesic Image Segmentation,” in *ECCV*, 2008.
- [7] C. Rother, V. Kolmogorov, and A. Blake, ““GrabCut”: Interactive Foreground Extraction Using Iterated Graph Cuts,” *ACM Trans. on Graphics*, vol. 23, no. 3, pp. 309–314, 2004.
- [8] G. Wang, M. A. Zuluaga, R. Pratt, M. Aertsen, T. Doel, M. Klusmann, A. L. David, J. Deprest, T. Vercauteren, and S. Ourselin, “Slic-Seg: A minimally interactive segmentation of the placenta from sparse and motion-corrupted fetal MRI in multiple views,” *Medical Image Analysis*, vol. 34, pp. 137–147, 2016.

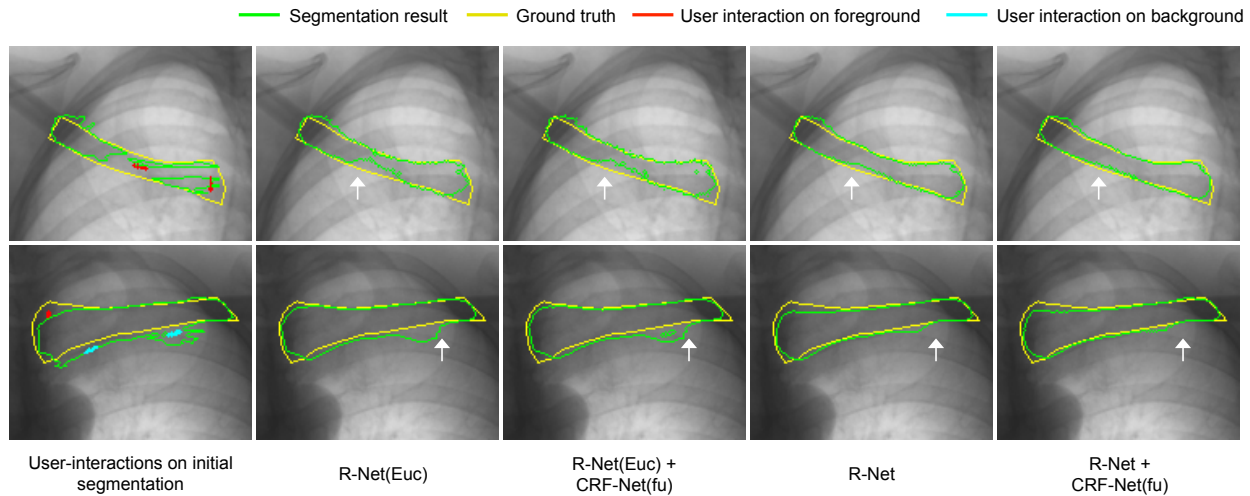


Fig. 13. Refinement of clavicle segmentation by R-Net with CRF-Net(fu). The first column shows the initial segmentation obtained by P-Net + CRF-Net(f), on which user interactions are added for refinement. The remaining columns show refined results. R-Net(Euc) is a counterpart of the proposed R-Net and uses Euclidean distance.

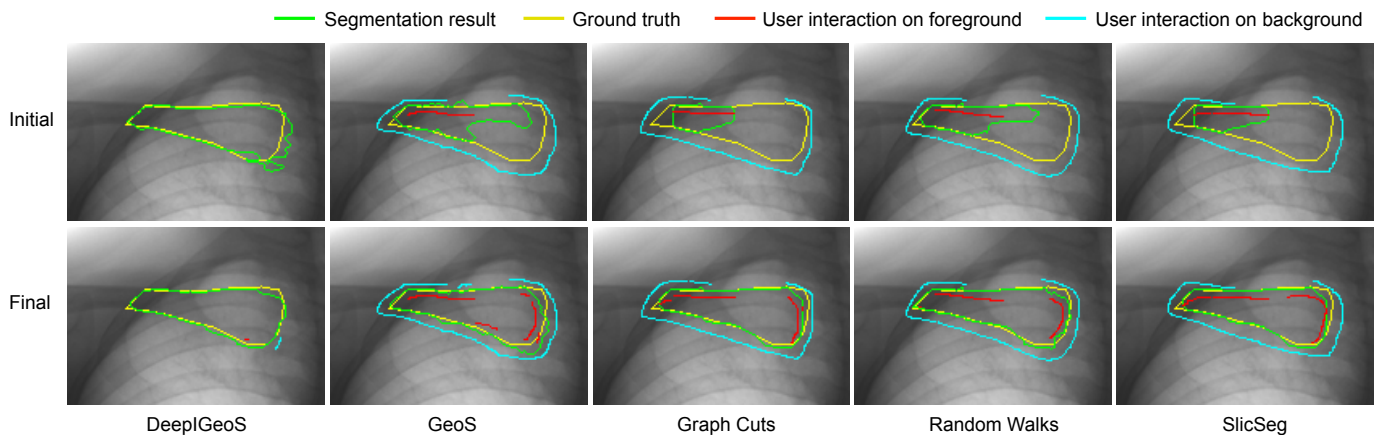


Fig. 14. Visual comparison of DeepGeoS and other interactive methods for clavicle segmentation. The first row shows initial scribbles (except for DeepGeoS) and the resulting segmentation. The second row shows final refined results with the entire set of scribbles. The user decided on the level of interaction required to achieve a visually acceptable result.

- [9] B. Wang, W. Liu, M. Prastawa, A. Irimia, P. M. Vespa, J. D. V. Horn, P. T. Fletcher, and G. Gerig, "4D active cut: An interactive tool for pathological anatomy modeling," in *ISBI*, 2014.
- [10] R. Girshick, J. Donahue, T. Darrell, and J. Malik, "Rich Feature Hierarchies for Accurate Object Detection and Semantic Segmentation," in *CVPR*, 2014.
- [11] J. Long, E. Shelhamer, and T. Darrell, "Fully Convolutional Networks for Semantic Segmentation," in *CVPR*, 2015, pp. 3431–3440.
- [12] L.-C. Chen, G. Papandreou, I. Kokkinos, K. Murphy, and A. L. Yuille, "Semantic Image Segmentation with Deep Convolutional Nets and Fully Connected CRFs," in *ICLR*, 2015.
- [13] M. Havaei, A. Davy, D. Warde-Farley, A. Biard, A. Courville, Y. Bengio, C. Pal, P.-M. Jodoin, and H. Larochelle, "Brain Tumor Segmentation with Deep Neural Networks," *Medical Image Analysis*, vol. 35, pp. 18–31, 2016.
- [14] K. Kamnitsas, C. Ledig, V. F. J. Newcombe, J. P. Simpson, A. D. Kane, D. K. Menon, D. Rueckert, and B. Glocker, "Efficient multi-scale 3D CNN with fully connected CRF for accurate brain lesion segmentation," *Medical Image Analysis*, vol. 36, pp. 61–78, 2017.
- [15] F. Yu and V. Koltun, "Multi-Scale Context Aggregation By Dilated Convolutions," in *ICLR*, 2016.
- [16] L.-C. Chen, G. Papandreou, I. Kokkinos, K. Murphy, and A. L. Yuille, "DeepLab: Semantic Image Segmentation with Deep Convolutional Nets, Atrous Convolution, and Fully Connected CRFs," *arXiv preprint arXiv:1606.00915*, 2016.
- [17] S. Zheng, S. Jayasumana, B. Romera-Paredes, V. Vineet, Z. Su, D. Du, C. Huang, and P. H. S. Torr, "Conditional Random Fields as Recurrent Neural Networks," in *ICCV*, 2015.
- [18] A. Abdulkadir, S. S. Lienkamp, T. Brox, and O. Ronneberger, "3D U-Net : Learning Dense Volumetric Segmentation from Sparse Annotation," in *MICCAI*, 2016.
- [19] D. Lin, J. Dai, J. Jia, K. He, and J. Sun, "ScribbleSup: Scribble-Supervised Convolutional Networks for Semantic Segmentation," in *CVPR*, 2016.
- [20] M. Rajchl, M. Lee, O. Oktay, K. Kamnitsas, J. Passerat-Palmbach, W. Bai, M. Rutherford, J. Hajnal, B. Kainz, and D. Rueckert, "DeepCut: Object Segmentation from Bounding Box Annotations using Convolutional Neural Networks," *TMI*, vol. PP, no. 99, pp. 1–1, 2016.
- [21] N. Xu, B. Price, S. Cohen, J. Yang, and T. Huang, "Deep Interactive Object Selection," in *CVPR*, 2016, pp. 373–381.
- [22] A. Krizhevsky, I. Sutskever, and G. E. Hinton, "ImageNet classification with deep convolutional neural networks," in *NIPS*, 2012.
- [23] C. Szegedy, W. Liu, Y. Jia, P. Sermanet, S. Reed, D. Anguelov, D. Erhan, V. Vanhoucke, and A. Rabinovich, "Going deeper with convolutions," in *CVPR*, 2015.
- [24] K. Simonyan and A. Zisserman, "Very deep convolutional networks for large-scale image recognition," in *ICLR*, 2015.
- [25] K. He, X. Zhang, S. Ren, and J. Sun, "Deep Residual Learning for Image Recognition," in *CVPR*, 2016.

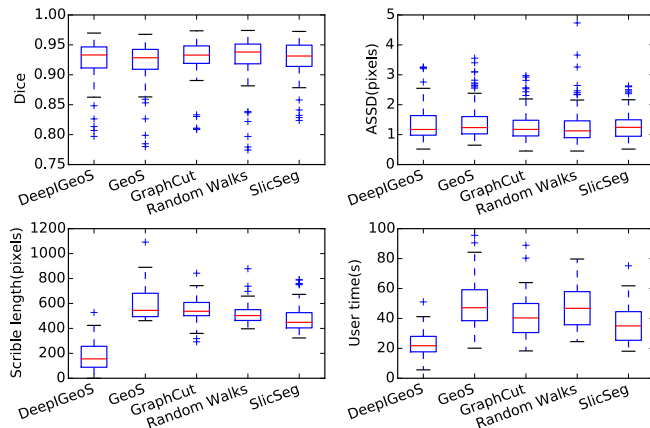


Fig. 15. Quantitative comparison of clavicle segmentation by different interactive methods in terms of Dice, ASSD, total interactions (scribble length) and the user's time.

- [26] A. Prason, K. Petersen, C. Igel, F. Lauze, E. Dam, and M. Nielsen, "Deep feature learning for knee cartilage segmentation using a triplanar convolutional neural network," in *MICCAI*, 2013.
- [27] B. Hariharan, P. Arbeláez, R. Girshick, and J. Malik, "Simultaneous Detection and Segmentation," in *ECCV*, 2014.
- [28] M. S. Hefny, T. Okada, M. Hori, Y. Sato, and R. E. Ellis, "U-Net: Convolutional Networks for Biomedical Image Segmentation," in *MICCAI*, 2015, pp. 234–241.
- [29] F. Milletari, N. Navab, and S.-A. Ahmadi, "V-Net: Fully Convolutional Neural Networks for Volumetric Medical Image Segmentation," in *IC3DV*, 2016, pp. 565–571.
- [30] P. Ondruska, J. Dequaire, D. Z. Wang, and I. Posner, "End-to-End Tracking and Semantic Segmentation Using Recurrent Neural Networks," in *Robotics: Science and Systems, Workshop on Limits and Potentials of Deep Learning in Robotics*, 2016.
- [31] J. Dai, K. He, Y. Li, S. Ren, and J. Sun, "Instance-sensitive Fully Convolutional Networks," in *ECCV*, 2016.
- [32] C. Lea, R. Vidal, A. Reiter, and G. D. Hager, "Temporal Convolutional Networks: A Unified Approach to Action Segmentation," in *ECCV*, 2016.
- [33] G. Lin, C. Shen, I. Reid, and A. van den Hengel, "Efficient piecewise training of deep structured models for semantic segmentation," in *CVPR*, 2016.
- [34] P. Pinheiro and R. Collobert, "Recurrent convolutional neural networks for scene labeling," in *ICML*, 2014.
- [35] B. Hariharan, P. Arbeláez, R. Girshick, and J. Malik, "Hypercolumns for object segmentation and fine-grained localization," in *CVPR*, 2015.
- [36] C. J. Armstrong, B. L. Price, and W. A. Barrett, "Interactive segmentation of image volumes with Live Surface," *Computers and Graphics (Pergamon)*, vol. 31, no. 2, pp. 212–229, 2007.
- [37] J. E. Cates, A. E. Lefohn, and R. T. Whitaker, "GIST: An interactive, GPU-based level set segmentation tool for 3D medical images," *Medical Image Analysis*, vol. 8, no. 3, pp. 217–231, 2004.
- [38] S. A. Haider, M. J. Shafiee, A. Chung, F. Khalvati, A. Oikonomou, A. Wong, and M. A. Haider, "Single-click, semi-automatic lung nodule contouring using hierarchical conditional random fields," in *ISBI*, 2015.
- [39] X. Bai and G. Sapiro, "A Geodesic Framework for Fast Interactive Image and Video Segmentation and Matting," in *ICCV*, oct 2007.
- [40] O. Barinova, R. Shapovalov, S. Sudakov, and A. Velizhev, "Online Random Forest for Interactive Image Segmentation," in *EEML*, 2012.
- [41] L. Wang, F. Shi, P. T. Yap, J. H. Gilmore, W. Lin, and D. Shen, "4D Multi-Modality Tissue Segmentation of Serial Infant Images," *PLoS ONE*, vol. 7, no. 9, 2012.
- [42] Y. Boykov and V. Kolmogorov, "An experimental comparison of min-cut/max-flow algorithms for energy minimization in vision," *PAMI*, vol. 26, no. 9, pp. 1124–1137, 2004.
- [43] J. Yuan, E. Bae, and X. C. Tai, "A study on continuous max-flow and min-cut approaches," in *CVPR*, 2010.
- [44] T. Toyoda and O. Hasegawa, "Random field model for integration of local information and global information," *PAMI*, vol. 30, no. 8, pp. 1483–1489, 2008.
- [45] P. Krähenbühl and V. Koltun, "Efficient inference in fully connected CRFs with gaussian edge potentials," in *NIPS*, 2011.
- [46] M. Szummer, P. Kohli, and D. Hoiem, "Learning CRFs using graph cuts," in *ECCV*, 2008.
- [47] J. I. Orlando and M. Blaschko, "Learning Fully-Connected CRFs for Blood Vessel Segmentation in Retinal Images," in *MICCAI*, 2014.
- [48] J. Domke, "Learning graphical model parameters with approximate marginal inference," *PAMI*, vol. 35, no. 10, pp. 2454–2467, 2013.
- [49] A. Adams, J. Baek, and M. A. Davis, "Fast high-dimensional filtering using the permutohedral lattice," *Computer Graphics Forum*, vol. 29, no. 2, pp. 753–762, 2010.
- [50] R. Vemulapalli, O. Tuzel, M.-y. Liu, and R. Chellappa, "Gaussian Conditional Random Field Network for Semantic Segmentation," in *CVPR*, 2016.
- [51] F. Liu, C. Shen, and G. Lin, "Deep Convolutional Neural Fields for Depth Estimation from a Single Image," in *CVPR*, 2014.
- [52] A. Kirillov, S. Zheng, D. Schlesinger, W. Forkel, A. Zelenin, P. Torr, and C. Rother, "Efficient Likelihood Learning of a Generic CNN-CRF Model for Semantic Segmentation," in *ACCV*, 2016.
- [53] P. Kohli, J. Shotton, and A. Criminisi, "GeoF Geodesic Forests for Learning Coupled Predictors," in *CVPR*, 2013.
- [54] V. Kolmogorov and R. Zabih, "What Energy Functions Can Be Minimized via Graph Cuts?" *PAMI*, vol. 26, no. 2, pp. 147–159, 2004.
- [55] D. Han, J. Bayouth, Q. Song, A. Taurani, M. Sonka, J. Buatti, and X. Wu, "Globally optimal tumor segmentation in PET-CT images: A graph-based co-segmentation method," in *IPMI*, 2011.
- [56] Y. Jia, E. Shelhamer, J. Donahue, S. Karayev, J. Long, R. Girshick, S. Guadarrama, and T. Darrell, "Caffe: Convolutional Architecture for Fast Feature Embedding," in *ACM/ICM*, 2014.
- [57] J. A. Deprest, A. W. Flake, E. Gratacos, Y. Ville, K. Hecher, K. Nicolaidis, M. P. Johnson, F. I. Luks, N. S. Adzick, and M. R. Harrison, "The Making of Fetal Surgery," *Prenatal Diagnosis*, vol. 30, no. 7, pp. 653–667, 2010.
- [58] A. Alansary, K. Kamnitsas, A. Davidson, M. Rajchl, C. Malamateniou, M. Rutherford, J. V. Hajnal, B. Glocker, D. Rueckert, and B. Kainz, "Fast Fully Automatic Segmentation of the Human Placenta from Motion Corrupted MRI," in *MICCAI*, 2016.
- [59] G. Wang, M. A. Zuluaga, R. Pratt, M. Aertsen, T. Doel, M. Klusmann, A. L. David, J. Deprest, T. Vercauteren, and S. Ourselin, "Dynamically Balanced Online Random Forests for Interactive Scribble-Based Segmentation," in *MICCAI*, 2016.
- [60] K. Keraudren, V. Kyriakopoulou, C. Malamateniou, M. A. Rutherford, B. Kainz, J. V. Hajnal, and D. Rueckert, "Automated Fetal Brain Segmentation from 2D MRI Slices for Motion Correction," *NeuroImage*, vol. 101, no. 1 November 2014, pp. 633–643, 2014.
- [61] K. Suzuki, H. Abe, H. MacMahon, and K. Doi, "Image-processing technique for suppressing ribs in chest radiographs by means of massive training artificial neural network (MTANN)," *TMI*, vol. 25, no. 4, pp. 406–416, 2006.
- [62] B. van Ginneken, M. B. Stegmann, and M. Loog, "Segmentation of anatomical structures in chest radiographs using supervised methods: a comparative study on a public database," *Medical Image Analysis*, vol. 10, no. 1, pp. 19–40, 2006.
- [63] L. Hogeweg, C. I. Sánchez, P. A. de Jong, P. Maduskar, and B. van Ginneken, "Clavicle segmentation in chest radiographs," *Medical Image Analysis*, vol. 16, no. 8, pp. 1490–1502, 2012.



Guotai Wang obtained his Bachelor and Master degree of Biomedical Engineering in Shanghai Jiao Tong University in 2011 and 2014 respectively. He then joined Transnational Imaging Group in UCL as a PhD student, working on image segmentation for fetal surgical planning. He won the UCL Overseas Research Scholarship and UCL Graduate Research Scholarship. His research interests include image segmentation, computer vision and machine learning.



Maria A. Zuluaga obtained her PhD degree from Universit Claude Bernard Lyon. After a year as a postdoctoral fellow at the European Synchrotron Radiation Facility (Grenoble, France), she joined CMIC, in March 2012, as a Research Associate to work on cardiovascular image analysis and computer-aided diagnosis (CAD) of cardiovascular pathologies. Since August 2014, she has been a part of the Guided Instrumentation for Fetal Therapy and Surgery (GIFT-Surg) project as a postdoctoral research associate.



Tom Doel is a Research Associate in the Translational Imaging Group at UCL and an Honorary Research Fellow at UCL Hospitals NHS Foundation Trust. His PhD at the University of Oxford developed computational techniques for multi-modal medical image segmentation, registration, analysis and modelling. He holds an MSc in applied mathematics from the University of Bath and an MPhys in mathematical physics from the University of Edinburgh. He is a professional software engineer and worked for Barco Medical Imaging Systems to develop clinical radiology software. His current research is on novel algorithm development and the robust design and architecture of clinically-focussed software for surgical planning and image-guided surgery as part of the GIFT-Surg project.



Wenqi Li is a Research Associate in the Guided Instrumentation for Fetal Therapy and Surgery (GIFT-Surg) project. His main research interests are in anatomy detection and segmentation for presurgical evaluation and surgical planning. Before joining TIG, he obtained a BSc degree in Computer Science from the University of Science and Technology Beijing in 2010, and then an MSc degree in Computing with Vision and Imaging from the University of Dundee in 2011. In 2015, he completed his PhD in the Computer

Vision and Image Processing group at the University of Dundee.



Anna L. David is a Professor and Honorary Consultant in Obstetrics and Maternal Fetal Medicine at Institute for Women's Health, University College London (UCL), London. She has a clinical practice at UCLH in fetal medicine, fetal therapy and obstetrics. Her main research is in translational medicine. She is Head of the Research Department of Maternal Fetal Medicine at UCL Institute for Women's Health.



Rosalind Pratt is a Clinical Academic Training Fellow at UCL Institute for Women's Health. She studied medicine at the University of Leeds, before starting clinical training in London, where she is undertaking specialist training in Obstetrics and Gynaecology. Her main research focus is in novel imaging of the human placenta.



Jan Deprest is a Professor of Obstetrics and Gynaecology at the Katholieke Universiteit Leuven and Consultant Obstetrician Gynaecologist at the University Hospitals Leuven (Belgium). He is currently the academic chair of his department and the director of the Centre for Surgical Technologies at the Faculty of Medicine. He established the Eurofoetus consortium, which is dedicated to the development of instruments and techniques for minimally invasive fetal and placental surgery.



Premal A. Patel is a Consultant Paediatric Interventional Radiologist at Great Ormond Street Hospital for Children NHS Foundation Trust and undertakes a variety of image guided procedures in children. He is also a Clinical Training Fellow within the Translational Imaging Group at UCL. He studied medicine at St Bartholomews and the Royal London Hospital School of Medicine and Dentistry, University of London. Following a period of training in Surgery and Paediatric Surgery in London, he undertook

training in Clinical Radiology in Southampton and subsequently undertook Fellowships in Paediatric Interventional Radiology at Great Ormond Street Hospital for Children, London, UK and The Hospital for Sick Children (SickKids), University of Toronto, Canada.



Sébastien Ourselin is Director of the EPSRC Centre for Doctoral Training (CDT) in Medical Imaging, Head of the Translational Imaging Group (TIG) as part of the Centre for Medical Image Computing (CMIC), and Professor of Medical Image Computing at UCL. His core skills are in medical image analysis, software engineering, and translational medicine. He is best known for his work on image registration and segmentation, its exploitation for robust image-based biomarkers in neurological conditions, as well as for his development of image-guided surgery systems.



Michael Aertsen is a Consultant Pediatric Radiologist at University Hospitals of Leuven. He studied medicine at the University of Hasselt and the Katholieke Universiteit Leuven. He is specialized in fetal MRI and his main research focus is the fetal brain development with advanced MRI techniques.



Tom Vercauteren is a Senior Lecturer within the Translational Imaging Group at UCL. He is a graduate from Columbia University and Ecole Polytechnique and obtained his PhD from Inria Sophia Antipolis. His main research focus is on the development of innovative interventional imaging systems and their translation to the clinic. One key driving force of his work is the exploitation of image computing and the knowledge of the physics of acquisition to move beyond the initial limitations of the medical imaging devices that are developed or used in the course of his research.